HHS Public Access

Author manuscript

Magn Reson Med. Author manuscript; available in PMC 2017 December 01.

Published in final edited form as:

Magn Reson Med. 2016 December ; 76(6): 1879–1886. doi:10.1002/mrm.26030.

Cardiac Magnetic Resonance Elastography of the Mouse: Initial Results

Yifei Liu[1], **Thomas J. Royston**[1,2,*], **Dieter Klatt**[2], and **E. Douglas Lewandowski**[2,3,4]

[1]Department of Mechanical & Industrial Engineering, University of Illinois at Chicago

[2]Department of Bioengineering, University of Illinois at Chicago

[3]Center for Cardiovascular Research, University of Illinois at Chicago

[4]Department of Physiology and Biophysics, University of Illinois at Chicago

Abstract

Purpose—Many cardiovascular diseases are associated with abnormal function of myocardial contractility or dilatability, which is related to elasticity changes of the myocardium over the cardiac cycle. The mouse is a common animal model in studies of the progression of various cardiomyopathies. This article introduces a novel non-invasive approach using microscopic scale magnetic resonance elastography to measure the myocardium stiffness change during the cardiac cycle on a mouse model.

Methods—A harmonic mechanical wave of 400 Hz was introduced into the mouse body. An electrocardiograph-gated and respiratory-gated fractional encoding cine-MRE pulse sequence was applied to encode the resulting oscillatory motion on a short-axis slice of the heart. Five healthy mice ages from 3 to 13.5 months were examined. The weighted summation effective stiffness of the left ventricle wall during the cardiac cycle were estimated.

Results—Results show the ratio of stiffness at end-diastole (ED) and end-systole (ES) in a range of 0.5 to 0.67. Additionally, variation in shear wave amplitude in the left ventricle wall throughout the cardiac cycle was measured and found to correlate with estimates of stiffness variation.

Conclusion—This study demonstrates the feasibility of implementing cardiac MRE on a mouse model.

Keywords

MRE; Elastography; cardiac MRE; mouse; left ventricle stiffness; myocardium

Introduction

Increased left ventricle (LV) stiffness, one of the contributing factors to abnormal systolic or diastolic function, has been found in various cardiovascular diseases (CVD) such as diastolic heart failure, cardiac fibrosis, steatosis, altered sarcomere activity and hypertension [1–5].

*Correspondence to: Thomas J. Royston, Ph.D., Department of Bioengineering, 851 S. Morgan Street Room 212, Chicago, IL 60607; troyston@uic.edu.

Conventionally, the primary approaches to assessing the contractility of the LV include an invasive method of measuring the pressure-volume (P-V) curves over the cardiac cycle [6,7] and noninvasive approaches of assessing deformation of the LV during systole and diastole, such as tagged MRI [8] or strain and strain rate echocardiography [9,10].

As a remote palpation method, MR elastography (MRE) is capable of estimating tissue stiffness or viscoelasticity non-invasively. MRE is a phase contrast-based MRI technique that observes the tissue response to a cyclic mechanical excitation. Subsequently, a map of the viscoelastic or stiffness properties of the targeted region of interest (ROI) is calculated with an appropriate inversion algorithm. MRE is a useful tool for the noninvasive mechanical characterization of soft biological tissues, including phantoms and engineered constructs [11,12], and the technique shows diagnostic potential for various diseases affecting different organs, such as the liver, brain, muscle, etc. [13–15].

Using MRE to noninvasively estimate the myocardium stiffness has been attempted in humans and large animals using a shear wave amplitude approach (WAV-MRE) [16–18] and using a shear wave inversion approach (WI-MRE) [19,20]. Both techniques indicate the diagnostic potential of cardiac MRE. The mouse model is a very common animal model in CVD studies [21,22], which can provide fundamental insight into disease progression and pathophysiology. While there have been numerous studies applying MRE to the mouse brain [23,24], there are few studies applying any form of noninvasive elastographic imaging to internal organs and deep structures within the torso of the mouse. This limited application is a consequence of the unique technical challenges associated with accounting for the rapid cardiac and respiratory cycles, in addition to the small dimensions. To the best of the authors' knowledge, the study presented here is the only published account of mouse cardiac MRE. MRE, which uses an external stimulus potentially enables quantitative and localized estimates of myocardial stiffness without the need for invasive catheterization. In this study, MRE was implemented on a healthy mouse model to assess the stiffness and shear wave amplitude change in the myocardium during the cardiac cycle. This study is challenging due to the fast heart beating rate (typically 500 beats/min) and small dimension of the mouse heart (typically less than 10 mm in all directions). The result is promising and demonstrates how myocardial stiffness and shear wave amplitudes change during the cardiac cycle.

Methods

Experimental setup

Five female adult C57BL/6 mice (age range 3–13.5 months, weight range 20–30 grams) were examined. The experiments conformed to our university Animal Care Committee (ACC) principles, and all the procedures were approved by the university ACC committee.

Mice were induced anesthesia with 5% vol. isoflurane in 1-liter oxygen flow for 3 min in an induction chamber and then were placed in a customized nonmagnetic cradle with a nose cone for inhaled anesthesia (1–1.5% vol. isoflurane at 1-liter oxygen flow), delivered with an isoflurane vaporizer machine (E-Z Anesthesia, E-Z System Corporation, PA). Mice were positioned supine in the cradle. The hair on the left thorax area was removed with Nair® depilating agent. A 3-D printed polylactic acid (PLA) plastic tube tip was then placed on the

chest above the heart as a passive driver as shown in Figure 1b. The right front paw and left back paw were connected to electrocardiogram (ECG) leads. A respiration pillow was placed and taped on the abdomen area.

All experiments were performed on a 9.4T Agilent (310/ASR, Santa Clara, CA) horizontal bore preclinical MR scanner with a self-shielded gradient coils (maximum strength 1000 mT/m) and a ϕ39 mm birdcage quadrature radiofrequency (RF) coil. The mouse along with the cradle was slid into the scanner. An air heating system (SA Instruments, Inc. NY) regulated the body temperature of the mouse and kept it around 37°*C*. The other end of the tube tip was connected to an acoustic speaker (11829BT, Electro Voice, MN, USA) located ~5 meters away from the magnet via several long rigid PVC pipes. The acoustic speaker was driven by an audio amplifier (P3500S, YAMAHA, Japan). The ECG, respiration and temperature signals were detected and monitored by an ERT control/gating module (SA Instruments, Inc. NY). The schematic of the experimental setup is shown in Figure 1a.

Image Acquisition

A gradient echo based cine-MRI sequences was upgraded with motion-sensitizing gradient (MSG) and prospective ECG triggering for cardiac cine-MRE. We adopt the concept of fractional encoding in order to combine rapid acquisition (and thus short MSGs) with low frequency vibrations. Fractional encoding has been introduced by Rump et al. [25]. In its cardiac MRE implementations one specific vibration state is estimated from successive repetition time (TR) intervals [17] which implies a condition for the MSG period (τ_g), the mechanical vibration period (τ_v) and the repetition time TR:

$$\tau_v = N \cdot TR; (N = 1, 2, 3 \ldots), \text{and } q = \frac{\tau_g}{\tau_v} < 1 \quad [1]$$

Due to the lower limit of our acoustic speaker (~280 Hz) and the need for a sufficient TR based on SNR considerations (a relatively longer TR is required due to the longer T1 under ultra-high magnetic field), we implemented fractional MRE with a vibration period τ_v that was shorter than the TR. This implementation violates Eq. 1 and therefore, we propose a data acquisition scheme that allows for arbitrary phase shifts of the vibration instead of phase-conformed in successive TR intervals. As illustrated in Figure 2, the vibration was activated by the R-wave ECG signal and was maintained for 1.5–2 cardiac cycles in expiration. During the active vibration, data were acquired for one line in k-space with 16–18 phases (number of phases depends on mouse heart beating rate) corresponding to different phases of the cardiac cycle. After the ECG trigger, a minimum vibration forerun of 20 ms was allowed before the start of the first phase for ensuring a mechanical steady state. After the last cardiac phase the vibration was turned off and the sequence of events was repeated for acquisition until the k-space was filled. Temporal resolution with eight time steps was achieved by increasing the forerun for consecutive image acquisitions by $\frac{1}{8}\tau_v$.

A short-axis slice was selected at the middle level of the LV for MR imaging. An MRE scan without acoustic actuation was performed as a control scan. Typical MRE sequence parameters were: FOV=2.5×2.5 cm with a 128×128 matrix; single slice of 1 mm slice

thickness; flip angle $\alpha = 20°$; 2 averages; 400 Hz of vibration; one cycle of a flow-compensated MSG with a strength of 20 Gauss/cm and duration of 1 ms. With timing parameters of TR/TE = 9.44/2.25 ms and a heart beating rate of 440~500 beats/min, the scan duration for one motion encoding direction was typically 12.5 minutes. The 3-D displacement vector was acquired by repeating the acquisition with varying MSG directions resulting in a total measurement time of 37.5 min for each data set.

Data Processing

Image post-processing was performed using MRElasto, a custom-written software using Matlab (an executable file is downloadable at http://avl-server.mie.uic.edu/AHP/htdocs/MRElasto_downloadpage.php). Phase-difference images were calculated to correct for static field inhomogeneity by subtracting phase images acquired with relative trigger shifts of $\frac{\tau_{vi}}{2}$. Subsequently, the complex wave image for each cardiac phase on each encoding direction was obtained after a Fourier-transform on the phase-difference images over one vibration cycle. A fourth order Butterworth bandpass filter with bandwidth of 1–30 waves/FOV plus an additional 2-D directional filter (four directions separated by 90°) were applied on the complex wave images to remove high-frequency noise and compensate for reflections [26]. Since data is available only in a single image slice, we are restricted to calculate the complex shear moduli G from the filtered complex wave images U using a 2-D direct inversion algorithm (Helmholtz inversion). The complex shear moduli $G_{j,n}(x, y, \omega)$ at cardiac phase #j on direction n (n = 1,2,3) were calculated from the filtered complex wave images $U_{j,n}(x, y, \omega)$ using a 2-D direct inversion algorithm (Helmholtz inversion) [27,28] shown in Eq. 2:

$$G_{j,n}(x,y,\omega)=\frac{-\rho\omega^2 U_{j,n}(x,y,\omega)}{\nabla^2 U_{j,n}(x,y,\omega)} \quad [2]$$

We determined for each cardiac phase an effective complex shear modulus G_{eff_j} as a weighted sum of the complex shear moduli along the three directions and the weighting coefficient is calculated from the direction-dependent displacements [29]:

$$G_{eff_j}(x,y,\omega)=\sum_{n=1}^{3} G_{j,n}(x,y,\omega)\cdot w_{j,n},\ w_{j,n}=\frac{|U_{j,n}(x,y,\omega)|}{\sum_{k=1}^{3}|U_{j,k}(x,y,\omega)|} \quad [3]$$

As a clarification, in this paper, when using the term “shear stiffness” to represent the estimation result of this mouse cardiac MRE study, it is the effective shear stiffness G_{eff} calculated from equation 3. In addition to the wave inversion based processing approach we also assess stiffness variations over the cardiac cycle by observing shear wave amplitude variations. We adopt the theory of Sack et al. [30], that the ratio of the wave amplitude $\bar{U}$ at two different time points t_1 and t_2 is inversely related to the ratio of stiffness μ under the assumption of a constant flux of the elastic wave energy:

$$\frac{\mu(t_1)}{\mu(t_2)}=\left(\frac{\overline{U}(t_2)}{\overline{U}(t_1)}\right)^4 \quad [4]$$

ROI selection

Due to the attenuation, the intrinsic contraction of the heart and the location of the excitation, the impact of the mechanical acoustic wave on the mouse body as well as the mouse heart varies from anterior to posterior locations. The wave amplitude therefore needs to be considered in deciding a suitable ROI for analysis. The wave amplitude can be calculated using Eq. 5:

$$\overline{U}_j(x,y,\omega)=\sqrt{\sum_{n=1}^{3}|U_{j,n}(x,y,\omega)|^2} \quad [5]$$

In order to identify regions of contracting tissue and to suppress static regions within the image, an empirical correlation map $\hat{S}$ is calculated according to Eq. 6 below [31]:

$$\hat{S}=\frac{1}{N}\sum_{j=1}^{N}\overline{U}_jS_j-\frac{1}{N^2}\sum_{j=1}^{N}\overline{U}_j\sum_{j=1}^{N}S_j;S=\begin{cases}0, & for\ systole\\ 1, & for\ diastole\end{cases} \quad [6]$$

where, N is the total number of the cardiac phases scanned and S is a step function determined by observing the duration of systole and diastole. The vibration amplitudes caused by a mechanical wave propagating in tissue depend (among other things) on the tissue stiffness [32]. Therefore, the expected amplitudes will not change over the cardiac cycle in regions that do not contract and Eq. 6 yields 0 for such a scenario. Thus the correlation map $\hat{S}$ compensates for the displacement amplitude of the unmoved region, and enhances the displacement amplitude of the region affected by both external mechanical vibration and the intrinsic contraction/dilation.

We examine correlations of cardiac phase and spatial averages of both wave inversion derived cardiac stiffness and shear wave amplitudes using three distinct ROIs. A semi-automatic ROI selection code is written in order to generate these ROIs for each cardiac phase. Three masks are generated in preparing the ROIs. A Mask #1 is automatically generated from the intensity of the MR magnitude images at each cardiac phase. A Mask #2 corresponds to the overall excitation affected map by adding up the wave amplitude images (Eq. 5) of all cardiac phases. The correlation map $\hat{S}$ obtained from Eq. 6 defines the two-dimensional Mask #3. Finally, the ROIs used for spatial averaging are defined as follows:

ROI 1: The LV manually selected from Mask #1.

ROI 2: The intersection of ROI 1, Mask #2 and Mask #3 using interactively selected thresholds to ensure sufficient wave energy and the inclusion of parts of the myocardium that are contracting.

ROI 3: The upper part of ROI 2 close to the source of the mechanical excitation.

See Figure 4 for an illustration of the ROI selection steps.

Results

Implementation and Representative Image Results

Individual MRE results shown in this section are primarily represented by experiments on mouse #5. Figure 1c and d show the comparison of the wave amplitude map of an MRE scan (Figure 1c) and its corresponding control scan without external actuation (Figure 1d) at the same cardiac phase (at ES). The figures are transparently overlapped with the magnitude image in order to identify the location of the left ventricle. From these figures, it can be observed that the excitation impacts the entire mouse body, and the red region indicates that the most affected area covered at least half of the left ventricle and was stronger in the region close to the actuation source.

The results of the same MRE scan above are given in Figure 3. Figure 3a and f are the magnitude images at end-systole (phase 3) and end-diastole (phase 9). Figure 3b~d and Figure 3g~i are the corresponding wave images for vertical, horizontal and out of plane motion-encoding directions, respectively. Figure 3e and j are the corresponding stiffness maps. An ROI of the entire left ventricle (ROI 1) was applied to the wave images and the stiffness maps and then overlapped on the magnitude images. All of the wave images use the same displacement scale, and motion can be observed in all of the three directions. This MRE scan has 18 cardiac phases and covered ~1.5 cardiac cycles. The curves of averaged stiffness and the wave amplitude over the three ROIs of each cardiac phase are given in Figure 4e. It can be observed that the LV stiffness increased during systole, and decreased during diastole with variations at a lower level during either of the two intervals of the cardiac cycle. Phase 3 and phase 14 were considered end-systole and phase 9 was considered end-diastole. Figure 4a~d illustrates the selection process of ROI 2 and ROI 3. Figure 4a gives the overall excitation-affected map of the MRE scan. The bright area shows the most affected region during the entire cardiac cycle. The region started from the upper chest, close to the excitation source, and spread into the body along the direction of the excitation, and covered at least half of the left ventricle. Figure 4b is the correlation map generated from Eq. 6. The high intensity correlation area covered most of the left ventricle and separated the left ventricle into two regions, upper and lower. From that ROI 2 was calculated as outlined in the methods section and ROI 3 represented the upper region of ROI 2 close to the vibration source. ROI 3 tends to be small, but it provides more accurate average amplitude. Figure 4c and Figure 4d illustrate ROI 3 at end-systole (phase 3) and at end-diastole (phase 9). The inverse proportional relation of stiffness and wave amplitude predicted by Eq. 4 is depicted by the result of ROI 3 (solid red line) in Figure 4e. It can be seen that the wave amplitude decreased during systole, and increased during diastole, which is inverse to the stiffness, as expected.

Grouped Data and Findings

ROI 1 and ROI 3 were examined for the MRE data of all mice in the study. The average stiffness results over the two ROIs at end-diastole and end-systole are given in Figure 5a. A box plot of the stiffness ratios μ_{ED}/μ_{ES} along with the amplitude ratio $(\mu_{ES}/\mu_{ED})^4$ from the results of these two ROIs is shown in Figure 5b. The ratio of the stiffness at end of diastole and end of systole is the factor that reflects the contractility of the left ventricle. A t-test was performed on the stiffness ratio versus the alternative that there is no stiffness change during the systole and diastole. The P value was found to be 8.5×10^{-5}.

The five mice in this study ranged in age from 3 to 13.5 months, weighed from 20 to 30 grams, and had a diameter of the left ventricle at middle level at the end of systole ranging from 4.9 to 5.5 mm, By comparing stiffness values of these five mice, no significant difference was found related to the age, weight or heart size. However, a final conclusion should be made with examination of more samples of mice with different ages and weights in a future study.

Discussion

Cardiac MRE on humans and in porcine models has been studied by other groups with different methods (WAV-MRE by Elgeti et al. [17,18] and WI-MRE by Kolipaka et al. [29]). However, in this study, for the first time, cardiac MRE is implemented in a mouse model and both WAV-MRE and WI-MRE processing approaches are applied. Our results suggest that the methods are useful for noninvasive detection of myocardial stiffness changes in the mouse and may therefore be valuable tools for monitoring cardiac disease progression and for testing therapies in mouse models of cardiac diseases.

Implementation of cardiac MRE on a mouse model is more challenging than on human or porcine models. The small size of the mouse body as well as the heart requires a relatively high frequency excitation. And, the small dimension of the preclinical MR scanner RF coil limits the available space for actuation setup. Multiple approaches with different excitation methods have been tried in this study, including using a piezo stack shaking a mouse bed with the mouse on it, or using a piezo stack driving a bent plastic rod to apply shear excitation directly to the mouse chest. Those approaches either could not provide enough excitation to the mouse heart or were harmful for the mouse. The custom-designed pneumatic system presented in this study provided the best excitation and least harm to the mouse. This design has also undergone multiple improvements for mouse comfort and excitation efficiency.

Also, frequency limits of this system imposed the need for a decoupling of TR and vibration period, which we successfully implemented in a modified fractional encoding pulse sequence. After removing the restriction of the vibration frequency, finding a workable excitation frequency is another factor that needs to be considered in this implementation. The small dimension of the mouse and the heart requires a high frequency excitation; however, high frequency vibration suffers from high attenuation with distance of penetration. Pre-tests with frequencies of 350 Hz, 400 Hz, 500 Hz, 800 Hz, and 1 kHz were conducted, and finite element simulations with different frequencies were performed as well

in this study [33] (not shown in here). The results showed the attenuation was too high in the region of interest at the higher frequencies; this led us to choose 400 Hz.

The ROI selection method in this study can more efficiently generate a reasonable ROI. The promising results of this study demonstrate the feasibility of MRE on the mouse heart. The stiffness of the left ventricle increased during systole, and decreased during diastole. And, the stiffness ratio matched the amplitude ratio to the power of 4 well when considering the correlated ROI 3.

However, limitations still exist in this technique. If heart rate varies greatly among the three scans, the cardiac phases at each of the three acquisitions will be unmatched, which could potentially bias the stiffness estimates. Furthermore, in order to obtain an accurate stiffness map for a complex geometry such as the mouse body, a 3-D inversion algorithm based on isotropic voxel multi-slice acquisition is required. Then the longitudinal wave can be removed by applying the curl operator to multi-slice data before using a 3-D inversion algorithm for calculation of stiffness maps. However, cardiac mouse MRE is restricted to single slice acquisitions due to the elongated scanning time with ECG and respiration gating at the current stage of development. And restriction to a 2-D plane is in contrast to the need for analyzing displacements along all three dimensions because of wave refraction and reflection within the torso. The approach of using a weighted sum of the complex shear moduli derived from 2-D scalar wave field inversion has yielded reasonable results in the presented study. However, 2-D inversion has its limitation that the shear stiffness accuracy is related to the ratio of the wavelength /pixel [28] and it is accurate only within relatively narrow bands within a larger volume [34]; either a faster multi-slice acquisition in cine-MRE needs to be developed or a more accurate algorithm should be derived in future studies.

Moreover, the boundary condition [35] is another factor that needs to be considered. In order to see how the boundary condition affects the result, erosion studies with different pixel depth of 1, 2 and 3 were performed, and results are shown in Figure 4e. It can be observed that with erosion, the amplitude did not have too much difference, but the stiffness increases with increasing erosion depth, although the trend of the stiffness changes still is consistent. However, a trade off of erosion and ROI area should also be considered because of the small area of the ROI. Take the scan presented in this study as an example; the area of ROI 3 changes from 89 pixels (no erosion) to 23 pixels (3 pixels erosion depth) at end of systole and 86 pixels (no erosion) to 7 pixels (3 pixels erosion depth) at end of diastole. Thus, choosing a reasonable erosion depth with a ROI of faithful size should also be considered in a future study. In this study, non-erosion was chosen due to the small area of the ROI.

Finally, the ROI selection is essential, especially with regard to the WAV-MRE processing approach. From the comparison of stiffness and wave amplitude over the three ROIs in Figure 4e, it can be observed that the wave amplitude curve only matches the trend of stiffness in ROI 3, while the stiffness keeps the same trend for all of the three ROIs, although has differences in values. Further, Figure 5e illustrates that similar ratio values for amplitude (4^{th} power) and stiffness as required by Eq. 4 are only obtained when using ROI 3. Thus, appropriate ROI selection is critical. A smaller area ROI with the same wave energy level

within the fully correlated ROI provides a more accurate result, which especially holds for the wave amplitude-based approach.

In summary, this study demonstrates the feasibility of cardiac MRE on a mouse model, and provides the possibility to use cardiac MRE in exploring more applications in cardiovascular disease studies.

Acknowledgments

This work was supported by NIH grant R01HL113057 (E.D.L.).

References

1. Zile MR, Baicu CF, Gaasch WH. Diastolic Heart Failure -- Abnormalities in Active Relaxation and Passive Stiffness of the Left Ventricle. New England Journal of Medicine. 2004; 350(19):1953–1959. [PubMed: 15128895]
2. Sinning D, Kasner M, Westermann D, Schulze K, Schultheiss H-P, Tschöpe C. Increased Left Ventricular Stiffness Impairs Exercise Capacity in Patients with Heart Failure Symptoms Despite Normal Left Ventricular Ejection Fraction. Cardiology Research and Practice. 2011
3. Benech JC, Benech N, Zambrana AI, Rauschert I, Bervejillo V, Oddone N, Damián JP. Diabetes increases stiffness of live cardiomyocytes measured by atomic force microscopy nanoindentation. American Journal of Physiology: Cell Physiology. 2014; 307(10):C910–C919. [PubMed: 25163520]
4. Conrad CH, Brooks WW, Hayes JA, Sen S, Robinson KG, Bing OHL. Myocardial Fibrosis and Stiffness With Hypertrophy and Heart Failure in the Spontaneously Hypertensive Rat. Circulation. 1995; 91:161–170. [PubMed: 7805198]
5. Hankiewicz JH, Banke NH, Farjah M, Lewandowski ED. Early impairment of transmural principal strains in the left ventricular wall after short-term, high-fat feeding of mice predisposed to cardiac steatosis. Circulation: Cardiovascular Imaging. 2010; 3:710–717. [PubMed: 20837747]
6. Burkhoff D, Mirsky I, Suga H. Assessment of systolic and diastolic ventricular properties via pressure-volume analysis: a guide for clinical, translational, and basic researchers. American Journal of Physiology: Heart and Circulatory Physiology. 2005; 289(2):H501–H512. [PubMed: 16014610]
7. Mirsky I, Pasipoularides A. Clinical assessment of diastolic function. Progress in Cardiovascular Diseases. 1990; 32(4):291–318. [PubMed: 2405455]
8. Bluemke DA, Boxerman JL, Atalar E, McVeigh ER. Segmented K-Space Cine Breath-Hold Cardiovascular MR Imaging: Part 1. Principles and Technique AJR American journal of Roentgenology. 1997; 169(2):395–400. [PubMed: 9242742]
9. Achenbach S, Friedrich MG, Nagel E, Kramer CM, Kaufmann PA, Farkhooy A, Dilsizian V, Flachskampf FA. CV Imaging: What Was New in 2012? JACC: Cardiovascular Imaging. 2013; 6(6):714–734. [PubMed: 23764098]
10. Dandel M, Lehmkuhl H, Knosalla C, Suramelashvili N, Hetzer R. Strain and Strain Rate Imaging by Echocardiography - Basic Concepts and Clinical Applicability. Current Cardiology Reviews. 2009; 5(2):133–148. [PubMed: 20436854]
11. Liu Y, Yasar TK, Royston TJ. Ultra wideband (0. 5–16 kHz) MR elastography for robust shear viscoelasticity model identification. Physics in Medicine and Biology. 2014; 59(24):7717. [PubMed: 25419651]
12. Yin Z, Schmid TM, Yasar TK, Liu Y, Royston TJ, Magin R. Mechanical characterization of tissue-engineered cartilage using microscopic magnetic resonance elastography. Tissue Engineering Part C: Methods. 2013
13. Manduca A, Oliphant TE, Dresner MA, Mahowald JL, Kruse SA, Amromin E, Felmlee JP, Greenleaf JF, Ehman RL. Magnetic resonance elastography: non-invasive mapping of tissue elasticity. Medical Image Analysis. 2001; 5(4):237–54. [PubMed: 11731304]

14. Sack I, Beierbach B, Wuerfel J, Klatt D, Hamhaber U, Papazoglou S, Martus P, Braun J. The impact of aging and gender on brain viscoelasticity. Neuroimage. 2009; 46(3):652–7. Epub 2009 Mar 10. [PubMed: 19281851]
15. Klatt D, Papazoglou S, Braun J, Sack I. Viscoelasticity-based MR elastography of skeletal muscle. Physics in Medicine and Biology. 2010; 55(21):6445. [PubMed: 20952814]
16. Elgeti T, Rump J, Hamhaber U, Papazoglou S, Hamm B, Braun J, Sack I. Cardiac Magnetic Resonance Elastography: Initial Results. Investigative Radiology. 2008; 43(11):762–772. [PubMed: 18923255]
17. Elgeti T, Sack I. Magnetic Resonance Elastography of the Heart. Current Cardiovascular Imaging Reports. 2014; 7(2):1–9.
18. Elgeti T, Knebel F, Hättasch R, Hamm B, Braun J, Sack I. Shear-wave Amplitudes Measured with Cardiac MR Elastography for Diagnosis of Diastolic Dysfunction. Radiology. 2014; 271(3):681–687. [PubMed: 24475861]
19. Kolipaka A, Araoz PA, McGee KP, Manduca A, Ehman RL. Magnetic Resonance Elastography as a Method for the Assessment of Effective Myocardial Stiffness Throughout the Cardiac Cycle. Magnetic Resonance in Medicine. 2010; (64):862–870. [PubMed: 20578052]
20. Kolipaka, A.; McGee, K.; Aggarwal, S.; Anavekar, N.; Manduca1, A.; Ehman, R.; Araoz, P. A Feasibility Study: MR Elastography as a Method to Compare Stiffness Estimates in Hypertrophic Obstructive Cardiomyopathy and in Normal Volunteers. 19th ISMRM; Montreal. 2011. p. 274
21. Zaragoza C, Gomez-Guerrero C, Martin-Ventura JL, Blanco-Colio L, Lavin B, Mallavia B, Tarin C, Mas S, Ortiz A, Egido J. Animal Models of Cardiovascular Diseases. Journal of Biomedicine and Biotechnology. 2011; 2011
22. Russell JC, Proctor SD. Small animal models of cardiovascular disease: tools for the study of the roles of metabolic syndrome, dyslipidemia, and atherosclerosis. Cardiovascular Pathology. 2006; 15(6):318–330. [PubMed: 17113010]
23. Riek K, Millward JM, Hamann I, Mueller S, Pfueller CF, Paul F, Braun J, Infante-Duarte C, Sack I. Magnetic resonance elastography reveals altered brain viscoelasticity in experimental autoimmune encephalomyelitis. NeuroImage: Clinical. 2012; 1(1):81–90. [PubMed: 24179740]
24. Clayton EH, Garbow JR, Bayly PV. Frequency-Dependent Viscoelastic Parameters of Mouse Brain Tissue Estimated by MR Elastography. Physics in medicine and biology. 2011; 56(8):2391–2406. [PubMed: 21427486]
25. Rump J, Klatt D, Braun J, Warmuth C, Sack I. Fractional encoding of harmonic motions in MR elastography. Magnetic Resonance in Medicine. 2007; 57(2):388–395. [PubMed: 17260354]
26. Manduca A, Lake DS, Kruse SA, Ehman RL. Spatio-temporal directional filtering for improved inversion of MR elastography images. Medical Image Analysis. 2003; 7(4):465–473. [PubMed: 14561551]
27. Mariappan YK, Glaser KJ, Ehman RL. Magnetic resonance elastography: A review. Clinical Anatomy. 2010; 23(5):497–511. [PubMed: 20544947]
28. Papazoglou S, Hamhaber U, Braun J, Sack I. Algebraic Helmholtz inversion in planar magnetic resonance elastography. Physics in Medicine and Biology. 2008; 53(12):3147. [PubMed: 18495979]
29. Kolipaka A, Aggarwal SR, McGee KP, Anavekar N, Manduca A, Ehman RL, Araoz PA. Magnetic Resonance Elastography as a Method to Estimate Myocardial Contractility. Journal of Magnetic Resonance Imaging. 2012; 36:120–127. [PubMed: 22334349]
30. Sack I, Rump J, Elgeti T, Samani A, Braun J. MR Elastography of the Human Heart: Noninvasive Assessment of Myocardial Elasticity Changes by Shear Wave Amplitude Variations. Magnetic Resonance in Medicine. 2009; 61:668–677. [PubMed: 19097236]
31. Elgeti T, Laule M, Kaufels N, Schnorr J, Hamm B, Samani A, Braun J, Sack I. Cardiac MR Elastography: Comparison with left ventricular pressure measurement. Journal of Cardiovascular Magnetic Resonance. 2009; 11(1):44. [PubMed: 19900266]
32. Achenbach, JD. Wave Propagation in Elastic Solids. North-Holland Publishing Company; 1973.
33. Liu, Y. High Resolution Cardiac Magnetic Resonance Elastography: From Phantom to Mouse Heart [Doctoral Dissertation]. Chicago: University of Illinois at Chicago; 2015. p. 143

34. Hamhaber U, Sack I, Papazoglou S, Rump J, Klatt D, Braun J. Three-dimensional analysis of shear wave propagation observed by in vivo magnetic resonance elastography of the brain. Acta Biomaterialia. 2007; 3(1):127–137. [PubMed: 17067861]

35. Murphy MC, Huston J, Jack CR, Glaser KJ, Senjem ML, Chen J, Manduca A, Felmlee JP, Ehman RL. Measuring the Characteristic Topography of Brain Stiffness with Magnetic Resonance Elastography. PLoS ONE. 2013; 8(12):e81668. [PubMed: 24312570]

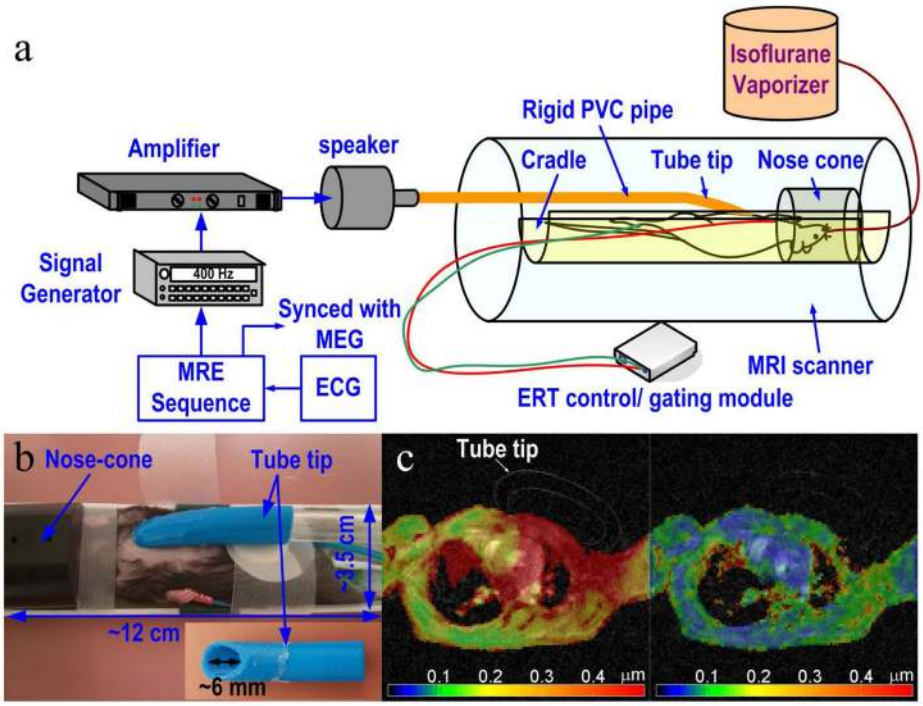

Figure 1.

a) Cardiac mouse MRE experimental setup. The mouse was positioned supine in a customized nonmagnetic cradle with a nose cone connected to an isoflurane vaporizer for inhaled anesthesia. A 3-D printed tube tip was placed on the left side of the chest of the mouse at one end and connected to an acoustic speaker at the other end via rigid PVC pipes. ECG, respiration and temperature signals were monitored by an ERT control/gating module; b) The photo of the mouse setup with the customized nose cone and the 3-D printed tube tip. c) and d) A confirmation of the excitation from this setup by comparing the wave amplitude image of an MRE scan (c) and a control scan (d) at the same cardiac phase (at ES) in mouse #5. The location of the actuator tip is tagged on the figure c. Intensity of the tip was weak in the magnitude images and therefore graphically highlighted in the figure.

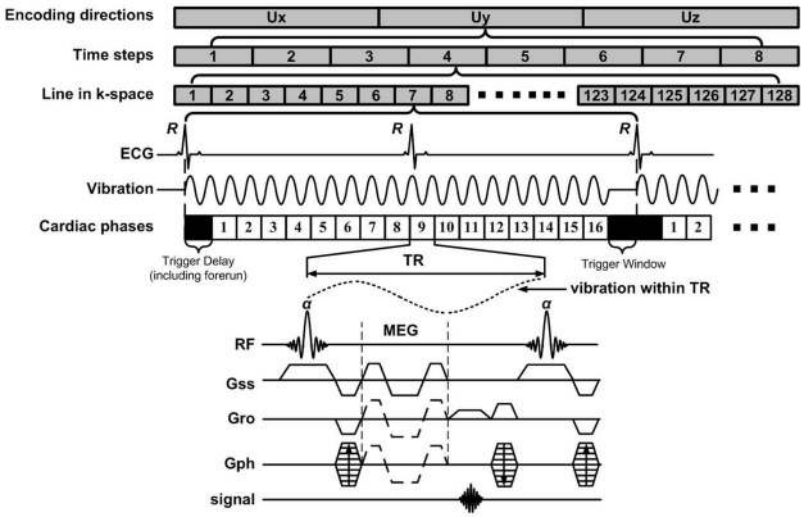

Figure 2.

A modified fractional encoding, prospective ECG-gated, gradient echo cine-MRE pulse sequence. The mechanical vibration is triggered with the R-wave ECG signal and is turned off immediately after the MSG of the last cardiac phase. The forerun time between the mechanical vibration trigger and the RF pulse of the first cardiac phase acquisition allows enough time for the acoustic wave to travel from the speaker to the mouse body and reach steady state. A flow compensated motion encoding gradient shape is applied to compensate for blood flow. More than 1.5 cardiac cycles are scanned in order to reconstruct the motion in at least one full cardiac cycle.

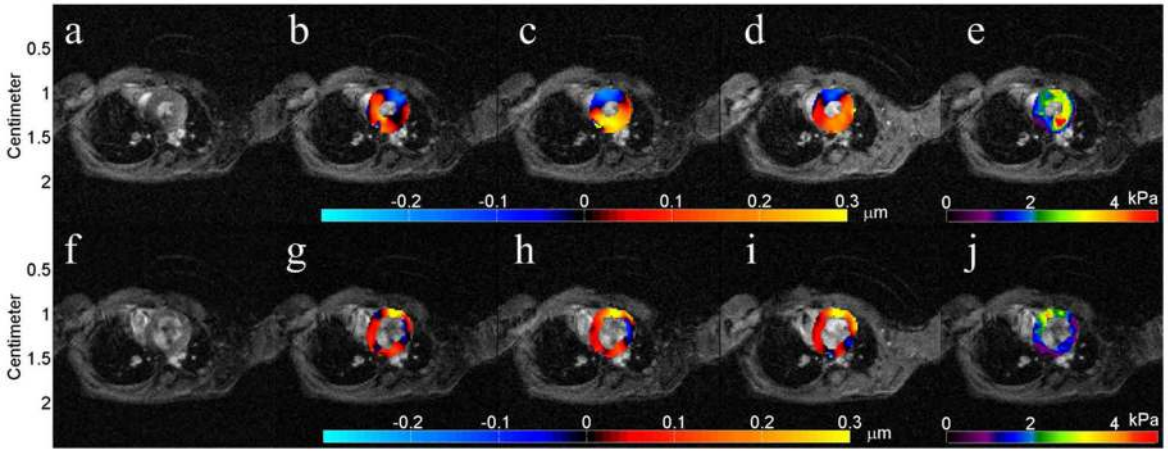

Figure 3.

A typical cardiac MRE scan result of the left ventricle. (a–e) shows the result at the end of systole (ES), where (a) is the magnitude image, (b–d) are the wave images at the three motion directions of vertical, horizontal and out of plane respectively, and (e) is the stiffness map of the left ventricle. (f–j) shows the result at the end of diastole (ED), where (f) is the magnitude image, (g–i) are the wave images at the three motion directions and (j) is the stiffness map of the LV.

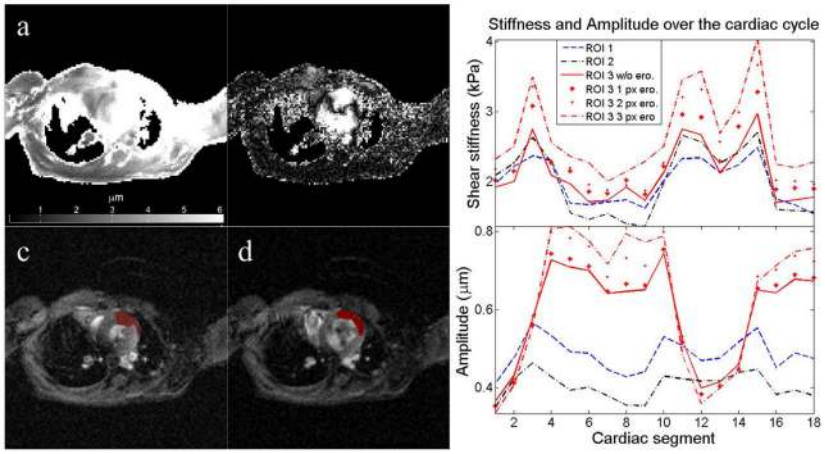

Figure 4.

a) The overall excitation affected map, which is the summation of the wave amplitude images of all cardiac phases; b) the correlation map generatated from equation 6; c) ROI 3 at end-systole; d) ROI 3 at end-diastole; e) the stiffness and wave amplitude change during the 18 cardiac phases (covered ~1.5 cardiac cycles) averaged over the ROIs: ROI #1: the entire LV; ROI #2: the full correlated region; ROI #3: the upper region of ROI #2, which was close to the chest, and the result with erosion of ROI # 3 with different eriosion depth (1, 2, and 3 pixels).

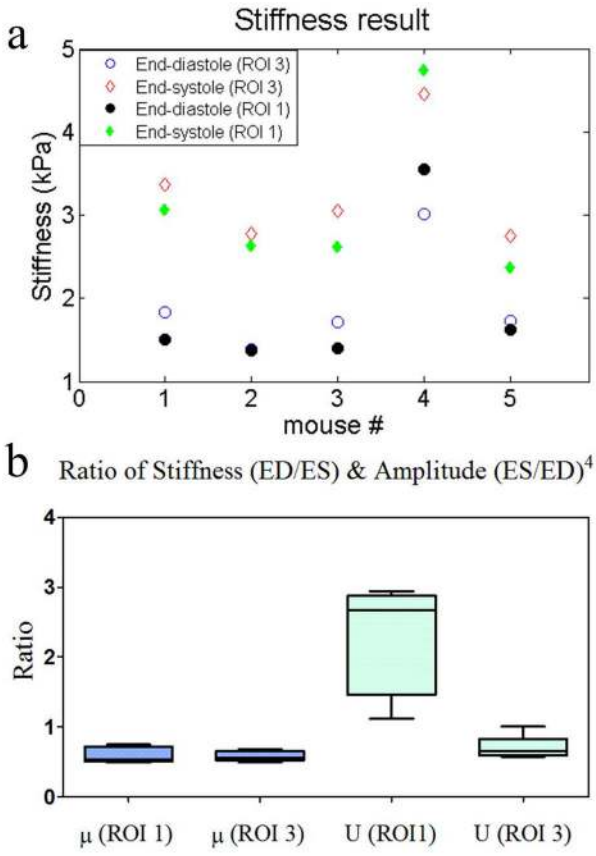

Figure 5.

a) Plot of the stiffness at ED and ES for the five mice, with two different ROI selections; b) Boxplot of the stiffness ratio μ_{ED}/μ_{ES} of the two ROIs (entire LV and the correlated map) and the wave amplitude ratio $(\mu_{ES}/\mu_{ED})^4$ of the correlated ROI of the five examined mice.